

# The enhancement of rapidly quenched galaxies in distant clusters at $0.5 < z < 1.0$

Miguel Socolovsky,<sup>1\*</sup> Omar Almaini,<sup>1</sup> Nina A. Hatch,<sup>1</sup> Vivienne Wild,<sup>2</sup>  
David T. Maltby,<sup>1</sup> William G. Hartley,<sup>3</sup> Chris Simpson<sup>4</sup>

<sup>1</sup>*School of Physics and Astronomy, University of Nottingham, Nottingham NG7 2RD, UK*

<sup>2</sup>*School of Physics and Astronomy, University of St Andrews, North Haugh, St Andrews, KY16 9SS, UK*

<sup>3</sup>*Department of Physics and Astronomy, University College London, 3rd Floor, 132 Hampstead Road, London NW1 2PS, UK*

<sup>4</sup>*Gemini Observatory, Northern Operations Center, 670 N. A‘ohoku Place, Hilo, HI 96720-2700, USA*

Accepted XXX. Received YYY; in original form ZZZ

## ABSTRACT

We investigate the relationship between environment and galaxy evolution in the redshift range  $0.5 < z < 1.0$ . Galaxy overdensities are selected using a Friends-of-Friends algorithm, applied to deep photometric data in the Ultra-Deep Survey (UDS) field. A study of the resulting stellar mass functions reveals clear differences between cluster and field environments, with a strong excess of low-mass rapidly quenched galaxies in cluster environments compared to the field. Cluster environments also show a corresponding deficit of young, low-mass star-forming galaxies, which show a sharp radial decline towards cluster centres. By comparing mass functions and radial distributions, we conclude that young star-forming galaxies are rapidly quenched as they enter overdense environments, becoming post-starburst galaxies before joining the red sequence. Our results also point to the existence of two environmental quenching pathways operating in galaxy clusters, operating on different timescales. Fast quenching acts on galaxies with high specific star-formation rates, operating on timescales shorter than the cluster dynamical time ( $< 1$  Gyr). In contrast, slow quenching affects galaxies with moderate specific star-formation rates, regardless of their stellar mass, and acts on longer timescales ( $\gtrsim 1$  Gyr). Of the cluster galaxies in the stellar mass range  $9.0 < \log(M/M_{\odot}) < 10.5$  quenched during this epoch, we find that 73% were transformed through fast quenching, while the remaining 27% followed the slow quenching route.

**Key words:** galaxies: evolution – galaxies: quenching – galaxies: environment, clusters – galaxies: high-redshift

## 1 INTRODUCTION

Galaxy properties, such as morphology and star formation activity, correlate with both environment (Dressler 1980; Kauffmann et al. 2004; Balogh et al. 2004; von der Linden et al. 2010; Haines et al. 2015) and the stellar mass of the galaxy (van der Wel 2008; Bamford et al. 2009). Massive galaxies and those in dense environments are predominantly spheroidal and quiescent, whereas lower mass and field galaxies are mainly disc-dominated and star-forming. Whilst these trends are most prominent in the present-day Universe, it has been shown that the preference for quiescent galaxies to reside in dense environments persists until at least redshift  $z \sim 1.5$  (Cooper et al. 2007; Chuter et al. 2011).

Peng et al. (2010) compare the stellar mass and environment of galaxies with their star formation rate (SFR), and conclude that there are two separate quenching processes that cause galaxies to cease forming stars. They call these processes “environmental quenching” and “mass quenching”. The efficiency of environmental quenching depends on the environment of a galaxy, such that galaxies in high density environments are more likely to be quenched. Independently, the efficiency of mass quenching correlates with the stellar mass of the galaxy, such that more massive galaxies are more likely to be quenched. Additionally, there is morphological quenching (Martig et al. 2009), in which the structure of the galaxy changes first, leading to a more stable configuration which prevents gas from collapsing into stars. However, the physical processes that are responsible for these quenching pathways remain unclear.

The most popular mechanisms used to explain mass

\* E-mail: ppxms4@nottingham.ac.uk

quenching include active galactic nuclei (AGN) feedback (Hopkins et al. 2005; Best et al. 2005), starburst-driven winds (Diamond-Stanic et al. 2012) and “hot halo” shock heating (Dekel & Birnboim 2006). Interactions between the intracluster or intergroup medium and galaxies, such as ram pressure stripping (Gunn & Gott 1972) and strangulation (Larson et al. 1980), are often invoked to explain environmental quenching, as are galaxy-galaxy interactions, such as harassment, mergers and tidal interactions. By measuring the timescale and efficiency of mass and environmental quenching, we can gain insight into where and when these processes act and which is the most important.

Several studies have investigated the timescale of environmental quenching. Semi-analytic models of galaxy formation required gas to be removed on long timescales ( $\sim 3\text{--}7$  Gyrs) to explain the fraction of passive satellites in clusters (Font et al. 2008; Kang & van den Bosch 2008; Weinmann et al. 2010; McGee et al. 2011; De Lucia et al. 2012; Wheeler et al. 2014). However, the rarity of transitional galaxies can only be explained if the quenching of star formation is rapid (Muzzin et al. 2012, 2014; Wetzel et al. 2012; Mok et al. 2013). Both observational constraints can be satisfied by a delayed-then-rapid quenching model (Wetzel et al. 2013). In this model galaxies experience a delay between the moment they become satellites and when their SFR starts to decline. This time delay can span over 2–4 Gyrs, but once the SFR begins to decline quenching occurs quickly ( $< 0.8$  Gyrs).

One approach to understanding the mechanisms responsible for quenching star formation in galaxies is to examine transitional galaxies. Post-starburst galaxies (PSBs), also referred to as “k + a” galaxies, are rare but valuable examples of galaxies caught in transition. Star formation in these galaxies has been rapidly truncated within the past  $10^9$  years. They exhibit a red spectral energy distribution (SED), but contain a residual population of A-stars that were born during the starburst phase (Dressler & Gunn 1983; Wild et al. 2009). These recently quenched galaxies may hold the key to understanding which processes are responsible for environmental and mass quenching.

Until recently, it was very difficult to identify PSBs at  $z > 0.5$  in large numbers (Yan et al. 2009; Vergani et al. 2010; Muzzin et al. 2014). The known sample of PSBs was limited because the PSB phase lasts only a short time, and large spectroscopic samples of optically-faint red galaxies are required to identify them. Recently, a new galaxy classification method has been developed by Wild et al. (2014) that only requires photometry. This method, based on a principal component analysis (PCA) of the photometry, has proven effective at classifying SEDs and allows for the identification of large samples of rare galaxies, such as PSBs. This method was verified by Maltby et al. (2016) who spectroscopically confirmed that 19 out of 24 ( $\sim 80\%$ ) photometrically-selected PSB candidates show genuine PSB features.

In this paper we investigate star-forming, passive and PSB galaxies in clusters and groups at  $0.5 < z < 1$  to understand the mechanisms responsible for environmental quenching during this period. In Section 2 we describe our data and galaxy classification method. In Section 3 we describe our method for identifying clusters. We note that our photometric method identifies only galaxy cluster and group candidates, but we nevertheless refer to them as “clus-

ters” throughout the rest of the paper. In Section 4 we compare our cluster sample with previous studies of clusters in the same field. We present our results in Section 5 and discuss their significance in Section 6. Finally, our conclusions are listed in Section 7. Throughout this paper we use AB magnitudes and we assume  $\Lambda$ CDM cosmology with the following set of parameters:  $\Omega_M = 0.3$ ,  $\Omega_\Lambda = 0.7$  and  $H_0 = 100 h \text{ kms}^{-1}\text{Mpc}^{-1}$  with  $h = 0.7$ .

## 2 DATA SETS AND GALAXY CLASSIFICATION

### 2.1 Galaxy catalogue

We use the *K*-band selected galaxy catalogue described in Hartley et al. (2013). This catalogue is based on the 8th data release of the Ultra Deep Survey (UDS; Almaini et al., in preparation) which covers an area of  $0.77 \text{ deg}^2$  to  $5\sigma$  depths of  $J=24.9$ ,  $H=24.2$  and  $K=24.6$ . The infrared imaging is complemented by deep optical imaging from the Subaru *XMM-Newton* Deep Survey (SXDS; Furusawa et al. 2008; Ueda et al. 2008), reaching  $5\sigma$  depths of  $B = 27.6$ ,  $V = 27.2$ ,  $R = 27.0$ ,  $i' = 27.0$  and  $z' = 26.0$ . In addition, our catalogue includes *U*-band imaging from the Canada-France-Hawaii Telescope (CFHT) to a  $5\sigma$  depth of  $U = 26.75$ , and near-infrared data from the *Spitzer* Legacy Program (SpUDS) ( $[3.6] = 24.2$  and  $[4.5] = 24.0$  at  $5\sigma$ ). The total combined survey area, after masking bright stars and other features, is  $\sim 0.62$  square degrees.

Stars are removed according to the criteria described in Simpson et al. (2013). The catalogue is limited to  $K < 24.3$  to ensure 95% completeness and the resulting catalogue consists of 23,398 galaxies at  $0.5 < z < 1.0$ .

### 2.2 Photometric redshifts and stellar masses

Photometric redshifts were derived by Simpson et al. (2013) using the EAZY photometric-redshift code (Brammer et al. 2008), fitting template spectra to the *U*, *B*, *V*, *R*,  $i'$ ,  $z'$ , *J*, *H*, *K*,  $3.6\mu\text{m}$  and  $4.5\mu\text{m}$  photometry. The photometric redshifts were tested against  $\sim 1500$  spectroscopic redshifts from the UDSz (ESO Large Programme, Almaini et al., in prep) and  $\sim 3500$  archival redshifts from the literature (Simpson et al. 2012). The resulting normalised median absolute deviation ( $\sigma_{\text{NMAD}}$ ) of  $z_{\text{phot}} - z_{\text{spec}}$  is  $\sigma_{\text{NMAD}} \sim 0.023$ .

The stellar masses of the galaxies were computed by Simpson et al. (2013) by fitting a grid of synthetic SEDs to the 11-band photometry assuming a Chabrier (2003) initial mass function (IMF). The redshift of each galaxy was fixed to the spectroscopic redshift, if known, otherwise derived properties were based on the photometric redshift.

### 2.3 Galaxy Classification and stellar ages

We use the galaxy classifications obtained from the PCA analysis described in Wild et al. (2016), which builds on the sample outlined in Wild et al. (2014). We refer the reader to those papers for a detailed description of the technique, but we provide a brief overview below, and define the various galaxy subclasses that are used in our work.

The aim of the PCA method was to characterise a broad

range of galaxy spectral energy distributions (SEDs) in a concise manner. It was found that a linear combination of three base SEDs (“eigenspectra”) was sufficient to describe the range of galaxy SEDs. The linear coefficients describing the contribution of each eigenspectrum to a given galaxy SED is termed a “supercolour” (SC).

The supercolour eigenvectors were determined using a grid of 44,000 model SEDs from the stellar population synthesis models of Bruzual & Charlot (2003), using stellar populations with stochastic star formation histories. These model SEDs are convolved with the corresponding photometric filters before the PCA is applied. Properties such as  $r$ -band light-weighted stellar ages, sSFRs and metallicities are obtained directly from these models. It was found that only three eigenvectors are required to characterise  $>99.9\%$  of the variance in our model SEDs. Supercolour SC1 alters the red-blue slope of the SED and traces the  $R$ -band weighted mean stellar age or sSFR. Supercolour SC2 modifies the strength of the Balmer break region, and traces the fraction of the stellar mass formed in bursts during the last billion years (burst fraction), and also correlates with metallicity. Supercolour SC3 also controls the shape of the SED around  $4000 \text{ \AA}$  and helps to break the degeneracy between metallicity and burst fraction.

Galaxies are classified based on their position in the resulting SC–SC diagrams (such as shown in Fig. 1). The boundaries between the populations were determined empirically by comparison to both spectroscopy and model SEDs (see Wild et al. 2014 for more details), and galaxies are divided into the following categories: star-forming (SF), passive (PAS), post-starburst (PSB), metal-poor and dusty galaxies (the last two are excluded from our sample). Wild et al. (2014) subdivide the SF population into 3 groups of decreasing sSFR: SF1, SF2, and SF3. For our work, we also split the PAS population into three populations of increasing mean stellar age, from PAS1 to PAS3. This dividing line was determined by splitting PAS galaxies along the vector  $(SC1, SC2) = (-5, -2)$ . The borders  $(SC2 = -\frac{5}{2}SC1 - 20)$  and  $(SC2 = -\frac{5}{2}SC1 - 31)$  are chosen so that they evenly split the PAS population into 3 subgroups. The locations of each of the 7 populations on the SC diagram are shown in Fig. 1.

In total, our galaxy catalogue consists of 11,625 SF1, 3,486 SF2, 2,055 SF3, 575 PAS1, 793 PAS2, 838 PAS3 and 418 PSBs to a magnitude limit of  $K < 24$  and in the range  $0.5 < z < 1.0$ . We calculate the 90% mass completeness limit for each type of galaxy using the method of Pozzetti et al. (2010). The mass limits at  $z = 1.0$  are  $10^{9.0}M_{\odot}$  for SF,  $10^{9.5}M_{\odot}$  for PAS and  $10^{9.3}M_{\odot}$  for PSB galaxy populations. In addition, in Section 3 we use a deeper (unclassified) galaxy sample to  $K < 24.3$  for the purposes of identifying galaxy overdensities. For the deeper sample, the 90% completeness limit as a function of redshift is described well by the following second-order polynomial:  $\log(M_*) \geq -0.41z^2 + 1.76z + 8.00$ .

As an important caveat, we note that we use the term “PSB” to refer to galaxies within the PSB region of the SC diagram. The majority (60–80%) of galaxies in this region of the diagram show spectroscopic “k+a” properties (Maltby et al. 2016), which means they have recently been rapidly quenched following significant star formation. As noted in Wild et al. (2016), however, this does not necessarily imply that they all underwent a “starburst” phase before quench-

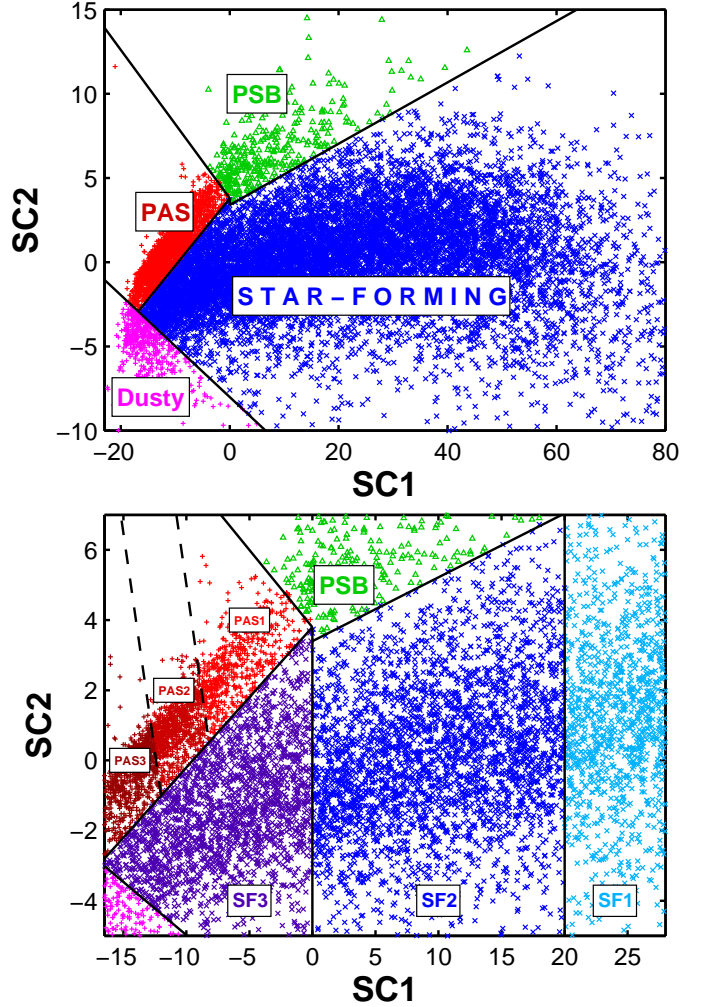


**Figure 1.** Top panel: the SC1–SC2 diagram for the galaxies in our sample, based on the PCA classification described in Wild et al. (2014). Galaxies belonging to different populations are represented in different colours. Solid black lines demarcate the borders between the main SC populations. Bottom panel: zoom in of the same diagram showing the sub-populations described in Section 2.3. Dashed black lines delimit the divisions of the passive galaxy region by mean stellar age.

ing. Very rapid quenching following a more extended period ( $< 3$  Gyr) of star formation may also produce these spectral features.

As a further caveat, we note that spectroscopic confirmation is so far confined to brighter galaxies ( $K < 23$ ), while a large fraction of our PSBs lie at slightly fainter limits ( $23 < z < 24$ ). Based on their SEDs, however, we have no reason to believe that the fainter PSB candidates show different characteristics, and they populate the PSB region of the SC diagram in the same way as the brighter counterparts. Additionally, we note that Maltby et al. (2016) exclude galaxies with  $W_{[\text{OII}]} < -5 \text{ \AA}$  to rule out PSB candidates with significant ongoing star formation. We acknowledge that galaxies with no significant [OII] have been found with residual  $H_{\alpha}$  emission (Yan et al. 2006), but the lack of [OII] together with strong higher order Balmer absorption lines (i.e.  $H_{\beta}$ ,  $H_{\gamma}$  and  $H_{\delta}$ ) is considered sufficient to rule out

significant ongoing star formation (Goto et al. 2003; Tran et al. 2003; Blake et al. 2004).

### 3 CLUSTER DETECTION METHOD

We use a Friends-of-Friends (FoF) algorithm (Huchra & Geller 1982; Geller & Huchra 1983; Merchán & Zandivarez 2005) to locate cluster and group candidates in the UDS. For brevity, we refer to candidate groups and clusters as “clusters” hereafter. The FoF method is characterised by three parameters: two linking distances, projected ( $d_{\text{link}}$ ) and along the line of sight ( $z_{\text{link}}$ ), and a detection threshold ( $N_{\text{min}}$ ), which is the number of member galaxies per structure. The algorithm starts by selecting one galaxy at  $[\mathbf{r}_0, z_0]$  from the catalogue which has not been assigned to any structure. All other galaxies fulfilling  $|\mathbf{r}_0 - \mathbf{r}_i| \leq d_{\text{link}}$  and  $|z_0 - z_i| \leq z_{\text{link}}$  are then designated as “friends”. The terms  $\mathbf{r}$  and  $z$  correspond to the position on the sky and redshift, respectively. The method is iterative and continues searching for friends of the friends until no remaining galaxy fulfils the conditions. The structure is classified as a cluster candidate if the number of linked galaxies is greater than  $N_{\text{min}}$ .

#### 3.1 Optimising the FoF algorithm

The completeness and contamination rates of the cluster sample strongly depend on the parameters  $d_{\text{link}}$ ,  $z_{\text{link}}$ , and  $N_{\text{min}}$ . We optimised these parameters to maximise the completeness of the cluster sample whilst also ensuring the cluster sample has no more than 5% contamination.

To estimate the contamination rate we ran the FoF algorithm on a mock galaxy catalogue using a range of FoF parameters. The mock catalogue had the same number, mean density, and redshift distribution of galaxies as in the UDS, but the RA and Dec were randomised so that the mock catalogue did not contain any groups or clusters. The contamination rate is defined as:

$$q_{\text{cont}} = \frac{N_{\text{mock}}}{N_{\text{UDS}}} \quad (1)$$

where  $N_{\text{mock}}$  is the number of clusters detected in the mock catalogue, and  $N_{\text{UDS}}$  is the number of clusters detected in the UDS using the same FoF configuration.

To determine the completeness rate, we injected mock clusters into the UDS catalogue and then attempted to recover them with the FoF algorithm. Mock clusters are constructed as  $N_{\text{sim}} = 20$  galaxies randomly distributed within an aperture of radius  $R_{\text{sim}} = 0.8$  Mpc. Each galaxy is assumed to have a stellar mass of  $M_* = 10^{10} M_{\odot}$ . These simplistic mock clusters result in a conservative estimate of the completeness as real clusters are typically more centrally concentrated, and therefore are easier to detect with a FoF algorithm. All mock clusters are placed at  $z_{\text{sim}} = 0.75$ , and redshift errors for each galaxy are simulated by randomly sampling a Gaussian distribution of dispersion equal to the photometric redshift uncertainty,  $\sigma_z = (1 + z)0.023$ .

We injected 100 mock clusters in low density regions of the UDS to prevent the mock clusters from overlapping with each other or with existing structures in the UDS. The FoF algorithm is then used to recover the mock clusters. The threshold for recovering a mock cluster is when at least 80%

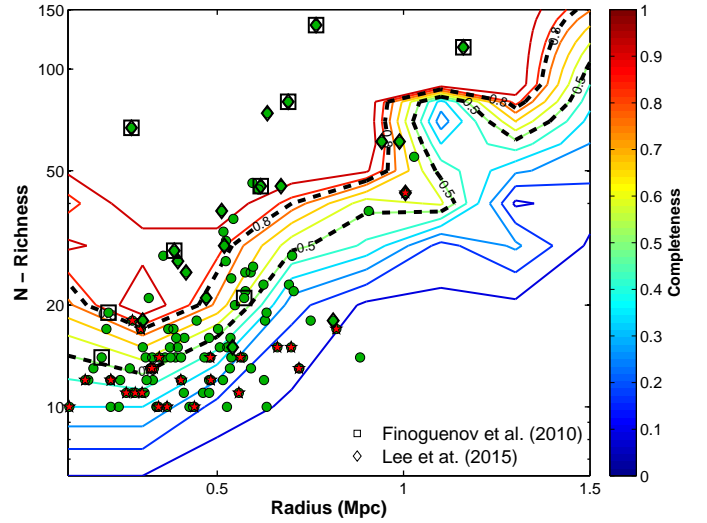


**Figure 2.** Completeness contours as a function of size and richness of clusters, based on simulated galaxy clusters. Contours of 50% and 80% completeness are highlighted with the thick dashed lines. The dots and stars represent cluster candidates from the UDS. Green dots represent good detections and red stars represent clusters excluded due to a large offset in the centre of mass or low  $S/N$  after background subtraction. In addition, cluster candidates coincident with published detections from Finoguenov et al. (2010) (boxes) and Lee et al. (2015) (diamonds) are included.

of the injected galaxies are detected and the offset of the centre of mass is less than a 30% of  $R_{\text{sim}}$ . The completeness rate ( $q_{\text{comp}}$ ) is defined as the ratio between number of successfully recovered clusters and the number of mock clusters injected into the simulation. A hundred of these simulations are run to obtain the average completeness rate of recovering 10,000 mock galaxy clusters.

We optimise the FoF algorithm by tuning the parameters to maximising the completeness-to-contamination ratio ( $r_{\text{comp/cont}}$ ) while keeping the value of  $q_{\text{cont}}$  low.

$$r_{\text{comp/cont}} = \frac{q_{\text{comp}}}{q_{\text{cont}}} \quad (2)$$

The best performing values are: a linking projected distance of  $d_{\text{link}} = 300$  kpc, and a linking distance along the line of sight of  $z_{\text{link}} = 40$  Mpc. At a minimum threshold of  $N_{\text{min}} = 10$  galaxies these parameters yield completeness and contamination rates of 31% and 5%, respectively.

#### 3.2 Limitations of the FoF algorithm

To test the limitations of our FoF cluster finding algorithm we estimated the recovery rate of mock clusters which have a variety of richness ( $N_{\text{sim}}$ ), size ( $R_{\text{sim}}$ ) and redshift ( $z_{\text{sim}}$ ). Fig. 2 shows that low-richness clusters are only detected if they are also compact. The completeness of our selection method decreases for clusters with small radii, as small deviations in the centre of mass position become significant compared to the size of the cluster. This means that the measured centre of mass for many of the mock clusters deviates from the true centre of mass by more than 30% of  $R_{\text{sim}}$ . However, this effect becomes important at implausibly small radii ( $< 100$  kpc), so it does not affect our results.

Fig. 2 shows that our method has low completeness for those clusters with fewer than 20 FoF member galaxies. However, this completeness is a lower limit because the mock clusters are less likely to be identified by the FoF algorithm due to the random, rather than centrally concentrated, spatial distribution of their member galaxies.

### 3.3 Cluster centre and effective radius

We define the projected centre of a cluster as the centre of mass of its FoF members, and its redshift is defined as the median of the photometric redshifts of its FoF members. The effective radius of a cluster,  $R_{0.85}$ , corresponds to the projected radius that encloses 85% of the stellar mass of the system.

The centre of a cluster can also be defined as the mean or median of the RA and Dec of all FoF members. The cluster centre should not depend strongly on the definition used, unless the cluster has no well-defined centre. Therefore, we remove 10 clusters from our sample whose measured centroid deviates by more than 30% of  $R_{0.85}$  depending on which definition is used (see Fig 3).

### 3.4 Cluster galaxy membership

The FoF algorithm is optimised to identify clusters in the UDS, but the galaxy membership of these clusters will be incomplete due to photometric redshift errors. To correct for missing galaxies, we define candidate cluster members as all galaxies within a cylinder around the centre of mass of each cluster. Each cylinder has a radius of  $R_{\text{cyl}} = 1$  Mpc, which is the typical size of a galaxy cluster, and a depth of  $\delta z_{\text{cyl}} = 2.5\sigma_z$ , which corresponds to  $\sim 250$  Mpc in our redshift range.

The large photometric redshift uncertainties means we must use long cylinders to avoid missing cluster galaxies, but this implies that the cylinders may include a significant fraction of field galaxies, which are considered contaminants. These contaminants can be removed by statistically subtracting the field galaxies expected in each cylinder.

### 3.5 Construction of a field galaxy sample

We construct a sample of field galaxies to remove the field contribution within the cylindrical volume containing the cluster members, and to use as second environment to compare with our cluster sample.

The field sample is constructed from the UDS. For each cluster cylinder, a field sample is defined as all galaxies in the UDS (which are not candidate cluster members) that lie within the same redshift interval as the cylinder. The number of galaxies in the field is then scaled by the ratio of unmasked pixels in the cluster region to the field region, so that the field corresponds to the same volume as the cluster, i.e. a cylinder with radius 1 Mpc and depth 250 Mpc. The rescaled field number count ( $N_{\text{Field}}^*$ ) can be expressed as the original number scaled by a normalisation factor,  $f$ :

$$N_{\text{Field}}^* = f N_{\text{Field}} = \frac{n_{\text{cyl}}}{n_{\text{Field}}} N_{\text{Field}} \quad (3)$$

where  $n_{\text{cyl}}$  is the number of good pixels inside the aperture corresponding to the cylinder and  $n_{\text{Field}}$  is the total number

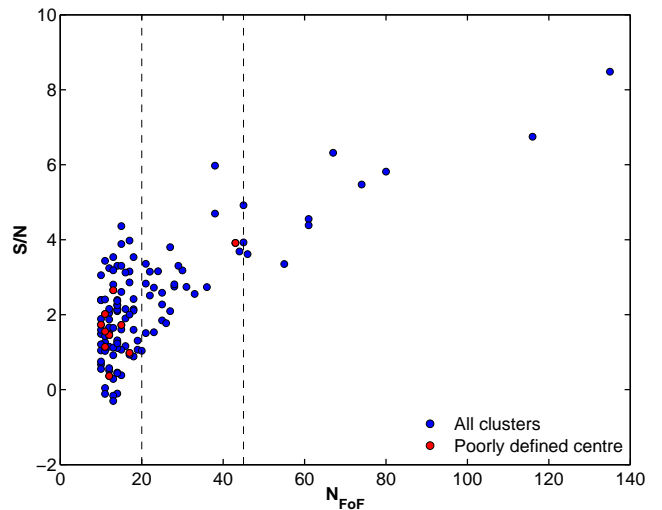


**Figure 3.** Signal-to-noise ( $S/N$ ) ratio of the cluster detections as a function of richness of our cluster sample, using the method described on Section 3.6. Dashed lines divide the richness into the three bins we utilise in the following sections. Clusters with poorly defined centres are shown as red dots, which seem to be concentrated in the lowest richness bin ( $N < 20$  galaxies), making this the most contaminated and unreliable regime.

of good pixels across the field sample. Finally, all the separate field regions corresponding to each detected cluster are combined together to produce the total field galaxy sample. We define a field sample for each cluster, but several clusters have similar redshifts so the total combined field sample contains some duplication of UDS galaxies. This duplication amounts to less than 10% of the total field sample.

### 3.6 Signal-to-noise ratio of the cluster detections

To determine a quality control for our cluster detections, we define the signal-to-noise ratio of each cluster detection as

$$S/N = \frac{N_{\text{cluster}} - f N_{\text{field}}}{\sqrt{\sigma_{\text{cluster}}^2 + \sigma_{\text{field}}^2}} = \frac{N_{\text{cluster}} - f N_{\text{field}}}{\sqrt{N_{\text{cluster}} + f^2 N_{\text{field}}}}, \quad (4)$$

where  $N_{\text{cluster}}$  is the number of galaxies in the cylindrical volume around the cluster,  $N_{\text{field}}$  is the number of galaxies in the field corresponding to the same redshift interval, and  $f$  is the scale factor that resizes the field to the cylindrical volume of the cluster.

Fig. 3 displays the richness (defined as the number of FoF members) and the  $S/N$  of our cluster sample. Richer clusters have a higher  $S/N$ . Only 3% of clusters with more than 20 members have poorly defined centres, whilst 17% of clusters with less than 20 member galaxies have poorly defined centres, and 25% have a  $S/N$  lower than unity. Based on both the low  $S/N$  and the low completeness rate found in Section 3.2, we decide to exclude those clusters with fewer than 20 member galaxies. This ensures a high quality cluster sample, although it significantly reduces the sample size.

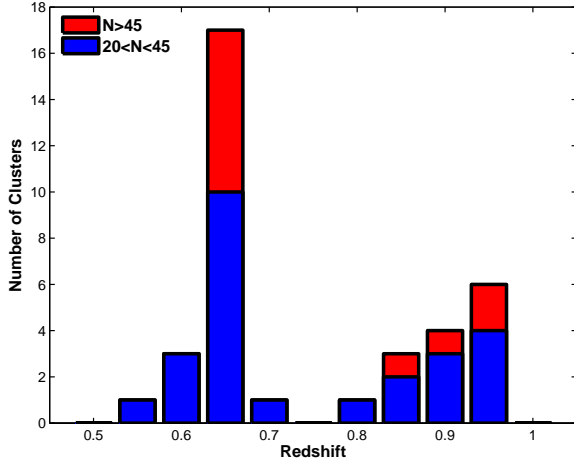


**Figure 4.** Distribution of detected clusters as a function of redshift. In the histogram red colour indicates clusters with more than 45 members and blue indicates clusters with more than 20 but less than 45 galaxy members.

## 4 CLUSTERS IN THE UDS

The FoF algorithm identifies 37 galaxy cluster candidates at  $0.5 < z < 1.0$  in the UDS field. Eleven cluster candidates contain more than 45 FoF members, whilst 26 have between 20 and 45 members. This results in a sample of 2210 cluster galaxies<sup>1</sup> (of which 98 are classified as PSBs) and 13,837 field galaxies (220 of which are PSBs). We also identify 87 cluster candidates with less than 20 and more than 10 FoF members, but we do not analyse these further as this sample has a high level of contamination.

The catalogue of our cluster candidates is provided in Table 1 and their redshift distribution is shown in Fig. 4. A spike in the redshift distribution of clusters is visible at  $z \sim 0.65$  due to the presence of a well-known galaxy overdensity, including a massive cluster in the CANDELS-UDS region (Geach et al. 2007). These structures are not fragments of the same massive cluster as they appear evenly spread across the UDS field. Instead, most of these structures are likely to be smaller clusters surrounding the massive cluster, since clusters of galaxies are highly clustered.

### 4.1 Spectroscopic confirmation of cluster candidates

To spectroscopically confirm our cluster sample, we utilise more than 6800 spectroscopic redshifts from the UDS field, including 1511 secure redshifts from the UDSz (ESO Large Programme, Almaini et al., in prep) and over 3000 archival redshifts from Subaru FOCAS and AAT 2dF (Akiyama et al. 2010; in prep), VLT VIMOS (Simpson et al. 2010; in prep), AAOMEGA (Smail et al. 2008) and VIPERS (Scodreggio et al. 2016). We classify a cluster as spectroscopically confirmed if it contains at least five spectroscopic galaxies within

<sup>1</sup> Cluster galaxies are defined as all the galaxies within the cylinder encompassing the cluster.

a cylinder of  $\pm 1000 \text{ km s}^{-1}$  length and 1 Mpc radius (Eisenhardt et al. 2008). In addition, the median of the spectroscopic cluster galaxies must not be offset by more than  $1\sigma$  from the photometric redshift of the candidate cluster. Eleven of our cluster candidates fulfil these conditions (see Table 1), of which three have not been previously presented in the literature.

### 4.2 Comparison with previous studies of clusters in the UDS

Clusters in the UDS have been located by Finoguenov et al. (2010) through the detection of extended *XMM-Newton* X-ray emission; by van Breukelen et al. (2006) and Lee et al. (2015), who searched for galaxy overdensities in the optical and near infrared photometric surveys, and by Geach et al. (2007), who used low-power radio galaxies as beacons for overdensities. We compare cluster samples derived from these methods with our FoF cluster sample to check the robustness of our detection method. Throughout this comparison, we use our whole sample of cluster candidates with a richnesses greater than 10 FoF galaxies. Although many of the cluster candidates with less than 20 FoF members are likely to be contaminants, some of them are expected to be real clusters, as shown by Fig. 2.

The two spectroscopically confirmed clusters at  $z = 0.65$  from Geach et al. (2007) are two of the most massive structures we select. We locate 83.3% (10/12) of the cluster candidates detected by van Breukelen et al. (2006), who used an algorithm based on FoF and Voronoi tessellation<sup>2</sup>. However, there seems to be a systematic bias in their cluster redshifts with respect to ours as theirs tend to be systematically lower at  $z > 0.7$ . This offset is probably due to the relatively unreliable photometric redshifts from the UDS DR1 catalogue used by van Breukelen et al. (2006), which was much shallower than the DR8 catalogue. We recover 85.2% (17/20) of the cluster candidates listed in Lee et al. (2015), where they locate clusters as galaxy overdensities in spatial and photometric redshift space. We also locate 78.5% (11/14) of the X-ray selected cluster candidates in Finoguenov et al. (2010). The 3 structures that we miss are close to our lower redshift limit at  $z = 0.514$ , 0.517 and 0.548.

Two X-ray selected cluster candidates at  $z = 0.548$  and  $z = 0.514$  (named SXDF66XGG and SXDF42XGG, respectively in Finoguenov et al. 2010) may be misclassified groups of X-ray AGN that are close in projection on the sky. No galaxy excess is detected near either of these cluster candidates. However, three *Chandra* X-ray point sources are located at angular separations of  $6.96''$ ,  $8.14''$  and  $15.20''$  from the centre of the SXDF66XGG cluster, each of them with a galaxy counterpart within 1 arcsec. Similarly, two X-ray point sources from the Subaru *XMM-Newton* Deep

<sup>2</sup> We define a cluster match if the RA and Dec of the cluster centre matches to within 2 arcmin ( $\sim 1 \text{ Mpc}$ ) and  $\Delta z \lesssim \sigma_z$ , where  $\sigma_z$  represent the total photometric redshift uncertainty i.e. the combination of the literature and our photometric redshift uncertainties. Furthermore, we ignore known or candidate clusters from the literature that fall within masked regions of our catalogue or lie outside our  $0.5 < z < 1.0$  redshift interval.

**Table 1.** Catalogue of galaxy cluster candidates detected in the UDS using the FoF algorithm. Identification number is provided in column 1, RA and Dec (2 – 3), photometric redshift (4). Column 5 corresponds to the median spectroscopic redshift of the spectroscopically confirmed clusters (see Section 4.1) and the number of spectroscopic redshifts associated with the structure (6). Three measurements of the richness of the clusters: number of FoF members (7), field subtracted number of galaxies within 1 Mpc from the cluster centre (8) and field subtracted stellar mass within 1 Mpc from the centre (9). Column 10 provides references if the structure has been previously detected. The bottom two rows correspond to clusters that are spectroscopically confirmed despite having fewer than 20 FoF members.

ID	RA (deg)	Dec (deg)	phot-z	median spec-z	N( $z_{\text{spec}}$ )	N <sub>FoF</sub>	N <sub>Sub</sub> (1 Mpc)	M <sub>Sub</sub> log( $M_*$ )	Reference
(1)	(2)	(3)	(4)	(5)	(6)	(7)	(8)	(9)	(10)
UDSC01FOF	34.70321	-5.14147	0.546			21	23	11.9312	<i>b</i>
UDSC02FOF	34.28647	-5.07732	0.609			22	22	11.2892	
UDSC03FOF	34.24918	-5.18202	0.618			21	13	11.8515	<i>a</i>
UDSC04FOF	34.64570	-4.96700	0.620	0.589	14	38	46	12.0126	<i>a, b</i>
UDSC05FOF	34.59033	-5.29313	0.627			28	25	11.9037	
UDSC06FOF	34.35261	-5.41159	0.628			45	52	12.1130	<i>b, c</i>
UDSC07FOF	34.42521	-5.46676	0.631			25	24	11.8822	
UDSC08FOF	34.18869	-5.14456	0.631			45	39	11.8729	<i>b</i>
UDSC09FOF	34.29001	-5.13710	0.632			27	18	11.8189	
UDSC10FOF	34.53183	-5.36065	0.635			27	38	11.8080	<i>a, b</i>
UDSC11FOF	34.67991	-5.38076	0.637			28	26	11.3117	
UDSC12FOF	34.28599	-5.42808	0.638			55	32	11.8175	
UDSC13FOF	34.58946	-5.38840	0.638			38	67	12.3032	
UDSC14FOF	34.39740	-5.22350	0.638	0.647	20	135	111	12.4485	<i>a, b, c, d</i>
UDSC15FOF	34.54191	-5.25419	0.641	0.647	10	74	57	12.2359	<i>b</i>
UDSC16FOF	34.60487	-5.41888	0.646	0.647	13	67	73	12.3414	<i>b, c, d</i>
UDSC17FOF	34.64400	-5.01744	0.648			44	36	11.8114	
UDSC18FOF	34.62682	-5.34075	0.651			31	25	11.6202	
UDSC19FOF	34.34840	-5.18454	0.651	0.649	10	24	30	11.8912	
UDSC20FOF	34.53353	-5.51288	0.671			43	36	11.8701	<i>b</i>
UDSC21FOF	34.49045	-5.45092	0.674	0.695	7	116	79	12.3302	<i>b, c</i>
UDSC22FOF	34.37161	-4.69193	0.681			25	15	11.4853	<i>b</i>
UDSC23FOF	34.21696	-5.20876	0.814			23	21	11.8909	<i>a</i>
UDSC24FOF	34.52203	-4.73357	0.850			30	27	11.9332	<i>a, b</i>
UDSC25FOF	34.82970	-5.08690	0.872	0.872	9	29	30	12.1240	<i>b, c</i>
UDSC26FOF	34.63429	-5.01229	0.874	0.874	31	80	67	12.3855	<i>a, b, c</i>
UDSC27FOF	34.36706	-4.70291	0.876			26	15	11.4445	
UDSC28FOF	34.71698	-5.35764	0.899			46	37	12.1644	
UDSC29FOF	34.27406	-5.16789	0.910			20	9	11.6155	
UDSC30FOF	34.76268	-4.70390	0.910			36	24	12.0208	<i>a</i>
UDSC31FOF	34.52417	-5.37735	0.918			25	22	11.7250	
UDSC32FOF	34.87913	-5.22070	0.926			23	12	11.9276	
UDSC33FOF	34.80408	-4.91053	0.926			21	33	11.9349	<i>c</i>
UDSC34FOF	34.34259	-5.20107	0.937	0.918	6	61	49	12.0711	<i>a, b</i>
UDSC35FOF	34.28586	-4.96203	0.953			33	27	11.8483	
UDSC36FOF	34.04102	-4.86472	0.953			61	50	12.1284	<i>b</i>
UDSC37FOF	34.28933	-4.76095	0.957			22	33	12.0459	<i>a</i>
UDSC38FOF	34.50443	-4.79895	0.568	0.583	14	13	22	11.9007	
UDSC39FOF	34.39913	-5.07272	0.800	0.801	10	13	25	11.9074	

<sup>a</sup> Detected by [van Breukelen et al. \(2006\)](#), <sup>b</sup> detected by [Lee et al. \(2015\)](#), <sup>c</sup> detected by [Finoguenov et al. \(2010\)](#), <sup>d</sup> detected by [Geach et al. \(2007\)](#)

Survey ([Akiyama et al. 2015](#)) are found within  $7.94''$  and  $10.70''$  from the centre of SXDF42XGG. These two sources have galaxy counterparts offset  $1.51''$  and  $3.81''$ , respectively, from the X-ray source, which is within the *XMM* point-source error circle.

The cluster candidate SXDF24XGG, at  $z = 0.517$ , shows a slight excess of galaxies in our catalogue. We detect the candidate as a group of 5 FoF galaxies when we optimise the algorithm to detect clusters at  $z \sim 0.5$ . When the algorithm is optimised to locate clusters across the redshift range  $0.5 < z < 1.0$  it begins to break down at both redshift extremes, but especially at low redshift. Hence, it is likely

that this small cluster is missed by our original detection algorithm.

We conclude that we do not detect all the X-ray cluster candidates from [Finoguenov et al. \(2010\)](#) because the presence of one or more X-ray point-sources (AGN) means that some cluster candidates are falsely identified as extended sources due to the low resolution of the *XMM-Newton* data. Furthermore, the X-ray cluster detection method is highly efficient at low redshift where our ability to detect clusters through the FoF algorithm decreases. This is supported by the test simulations shown in Fig. 2 where some X-ray

cluster candidates lie in the low completeness regime of our method.

## 5 RESULTS

In this section we compare the properties of galaxies identified in our 37 candidate galaxy clusters with those identified in the field, focussing on the redshift range  $0.5 < z < 1.0$ . The “cluster” sample consists of galaxies identified in overdense regions containing at least 20 members, linked by the Friends-of-Friends algorithm, as described in Section 3.

In Section 5.1 we compare the PCA supercolours for the cluster and field samples, while in Section 5.2 we compare the stellar mass functions. In Section 5.3 we investigate the radial distribution of galaxies for the cluster populations.

### 5.1 Cluster and field galaxy populations

In Fig. 5 we present the number density of galaxies across the SC1–SC2 diagram for our candidate galaxy clusters and the field. For the cluster sample, the densities across the SC diagram are obtained after subtracting the corresponding values for the field (correcting for the volumes sampled), to correct for the contamination from field galaxies in the cluster volumes. We find significant differences between the cluster and field populations, which are emphasized in the final panel, which displays the difference between the cluster and field regions.

We observe that galaxies in clusters are, in general, more evolved than those in the field. The differences are reflected in the overall shift of cluster galaxies towards the left side of the SC-diagram, producing an enhancement of the quiescent galaxies (PAS) and star-forming galaxies in the SF3 class, characterised by their high mean stellar ages and low sSFRs. Following the same trend, there is a lack of young star-forming objects in clusters (at high values of SC1). The SF1 class, with the highest sSFR, is common in the field but rare in clusters.

There are PSBs in both environments, but their distributions over the SC-space is significantly different. While PSBs in the field are found to be widespread over the upper region of the diagram, their counterparts in dense environments only populate the area closest to the border with the PAS population ( $SC2 < 10$ ). A two-sample Kolmogorov-Smirnov (KS) test applied only to SC2, rejects the null hypothesis that the field and cluster PSBs are drawn from the same underlying distribution (giving a probability of  $1.45 \times 10^{-6}$ ). This difference may suggest that PSBs are formed via different mechanisms, depending on their environment. We explore this result and its possible implications in Section 6.3.

### 5.2 Mass Functions of clustered galaxies vs. the field

Stellar mass functions can provide further information on the evolution of galaxies and, in particular, about the range of masses affected by environmental quenching. In this section we present the stellar mass functions of SF, PAS and PSB galaxies split by environment. Additionally, we split the SF category by decreasing sSFR (SF1, SF2 and SF3)

and the PAS sample by increasing mean stellar age (PAS1, PAS2, PAS3), using the classification boundaries defined in Section 2.3.

The stellar mass functions shown in Fig. 6 are computed using the cluster and field samples. Since the cluster total densities are arbitrary, given that the volume of the cylinder is chosen artificially, the cluster mass functions are normalised so that the total density (of all galaxies) matches the total density in the field. This allows us to compare the shapes of the mass functions across environments and populations, but implies that a comparison of normalisations (i.e. total densities) is only meaningful within the same environment. Although the normalisation is arbitrary, all densities are offset by the same amount from the true cluster density; we parametrise this offset by introducing the quantity  $\xi$  whose exact value is unknown to us.

$$\xi = \frac{\text{total density in clusters}}{\text{total density of the field}} \quad (5)$$

Cluster galaxy mass functions are computed using the cluster sample described in Section 4, consisting of 37 candidate clusters at  $0.5 < z < 1.0$  with more than 20 members linked by the FoF algorithm. The field mass function is subtracted in order to remove background contamination. We fit simple Schechter functions to all our mass functions except to the cluster PSBs, to which we fit a double Schechter mass function, with two power laws and one exponential (Pozzetti et al. 2010). This is because we believe the cluster PSB class comprises two different populations; one which is identical to that observed in the field and one that is produced by environmental quenching (see also Wild et al. 2016). The list of fitted Schechter parameters is given in Table 2. Fits were performed using a Maximum Likelihood method using unbinned data (Marshall et al. 1983).

The stellar mass functions of the three main populations show significant differences as a function of environment, with PSBs showing the largest difference between clusters and the field. The probability (p-value) of both populations being drawn from the same distribution according to a KS test is  $p_{KS} = 4.2 \times 10^{-6}$ . The stellar mass function of this population suggests that they are very strongly clustered, as the number density is more than  $3 \xi$  times larger in clusters than in the field. The shape of the mass function is also very different; PSBs in clusters are predominantly low-mass galaxies ( $M < 10^{10.5} M_{\odot}$ ) while in the field the range of masses is broader.

The PAS population also shows a strong environmental dependence. Passive galaxies are more abundant in clusters, as expected, with  $2.5 \xi$  times the density of the field. More interesting is the different shape of the passive galaxy mass function in clusters with respect to the field, with evidence for an excess of low-mass galaxies; we reject the null hypothesis that the populations are drawn from the same underlying distribution at significance  $p_{KS} = 9.9 \times 10^{-3}$ . Furthermore, we see that this excess is mainly produced by the “younger” passive galaxies (i.e. the most recently quenched), with PAS1 presenting  $p_{KS} = 1.4 \times 10^{-4}$  between field and cluster.

The SF population also presents a stellar mass distribution that depends on environment ( $p_{KS} = 3.6 \times 10^{-9}$ ), with a deficit of low-mass galaxies in cluster environments. Unlike the PAS and PSB populations, the overall density

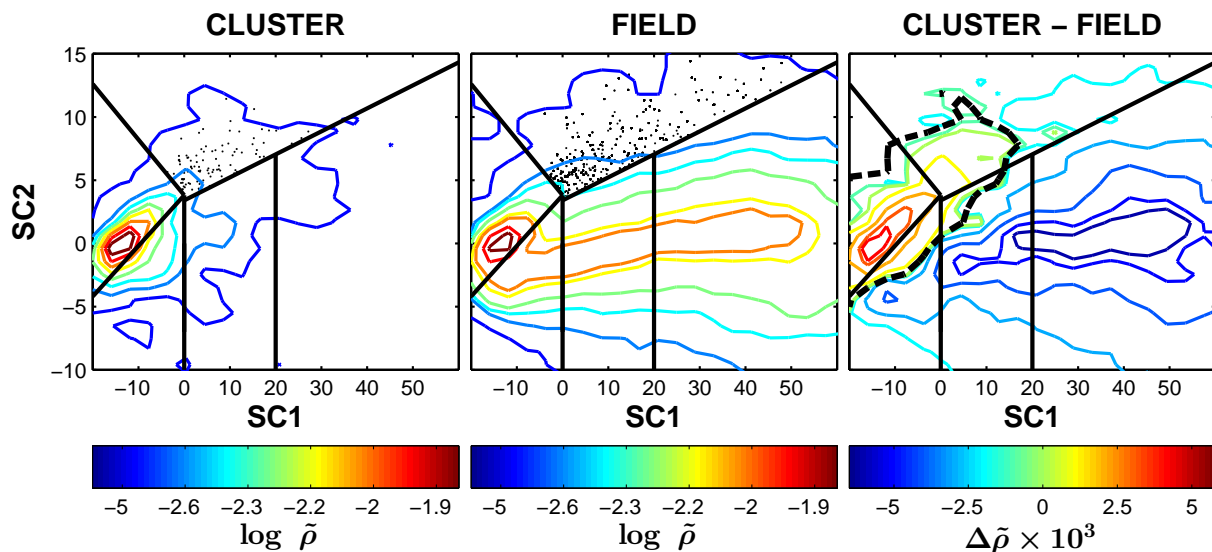


**Figure 5.** The distribution of UDS galaxies at  $0.5 < z < 1.0$  across the SC-space. Straight solid black lines represent the boundaries between the different galaxy populations and black dots the PSBs in the sample. Colour contours show the number of galaxies per bin normalised by the total number of galaxies in the diagram, where the bin size is  $\Delta\text{SC1} \times \Delta\text{SC2} = 4 \times 1$ . The panel on the left shows the distribution of cluster galaxies (note it has been field subtracted). The central panel shows the distribution of field galaxies. The right-hand panel shows the difference between cluster and field densities, with the dashed black contour representing the regime where field and cluster have the same density.

in the field is  $\sim 1.2 \xi$  times higher than in clusters, which indicates that SF galaxies have no preference for dense environments. Some studies have found the opposite trend, suggesting a high fraction of star-forming galaxies in dense environments at  $z \sim 1$  (Elbaz et al. 2007; Cooper et al. 2008). However, these were conducted using optical galaxy selection, which has been shown to be strongly biased towards blue star-forming galaxies at high redshift. With the rise of near-infrared surveys, it was found that the star formation–density relation was in place already at  $z \sim 1\text{--}1.5$  (Williams et al. 2009; Chuter et al. 2011).

Studying the three SF sub-populations we find a strong dependence of quenching with both sSFR and stellar mass. The population with the highest sSFR (SF1) is found to be strongly suppressed in clusters. This suppression is also mass-dependent and is more efficient at low stellar masses; a KS test rejects the null hypothesis that mass distributions in clusters and the field are drawn from the same underlying population ( $p_{\text{KS}} = 3.1 \times 10^{-8}$ ). For the intermediate class (SF2) we find a slight suppression in the relative number density in cluster environments, but no evidence for a change in the shape of the mass function. In contrast to SF1 galaxies, the relative abundance of the SF3 population appears to be enhanced in cluster environments, with evidence for an excess of low-mass galaxies in particular; a KS test rejects the null hypothesis that the mass functions are drawn from the same underlying population with  $p_{\text{KS}} = 1.4 \times 10^{-3}$ .

For the purpose of estimating timescales (see Section 6.1) we also evaluate the mass functions of those PAS1 galaxies which were quenched during the epoch  $0.5 < z < 1.0$  (based on mean stellar age from SC fits). This sub-population is shown in magenta (clusters) and cyan (field) in the lower-left panel of Fig. 6. We find that cluster galaxies satisfying this condition are systematically less massive than when the whole sample was employed. This means that the

most recently quenched objects are mostly low-mass galaxies, and the most massive PAS galaxies were likely to have been in place already by  $z = 1$ . This sharpens the apparent difference between cluster and field PAS1 galaxies, based on a KS test ( $p_{\text{KS}} = 1.4 \times 10^{-13}$ ).

Summarising this section, we find an excess of low-mass galaxies among the PAS, PSB and SF3 populations in clusters. In contrast, we find that galaxies with high sSFR (SF1 and SF2) are suppressed in such environments. Additionally, the quenching of high sSFR galaxies in clusters seems to be mass-dependent, affecting low-mass galaxies more efficiently than massive systems.

### 5.3 Radial distribution of galaxies in clusters

The radial distribution of different galaxy populations in clusters can, in principle, provide information on where quenching is taking place and the likely timescales. We define the centre of a cluster as its centre of mass and measure projected distances to all galaxy members within 1 Mpc. Additionally, clusters are split in two richness bins ( $20 < N_{\text{FoF}} < 45$  and  $N_{\text{FoF}} > 45$  members) to reduce the influence due to variation in size, and stacked together to produce radial profiles.

The radial trends of all PAS galaxies, PSBs and SF1s are shown in Fig. 7. We plot only SF1 instead of the total SF population because, as the mass functions demonstrated, this population has the strongest environmental dependence.

The radial plots show the expected trends for the star-forming and quiescent galaxies. As in previous studies, red passive galaxies tend to reside in the inner, denser regions of the clusters while blue star-forming galaxies prefer the outskirts and dominate at large cluster-centric distances (Oemler 1974; Muzzin et al. 2014). This difference is reflected in a KS test, which gives rise to  $p_{\text{KS}} = 1.2 \times 10^{-12}$  and

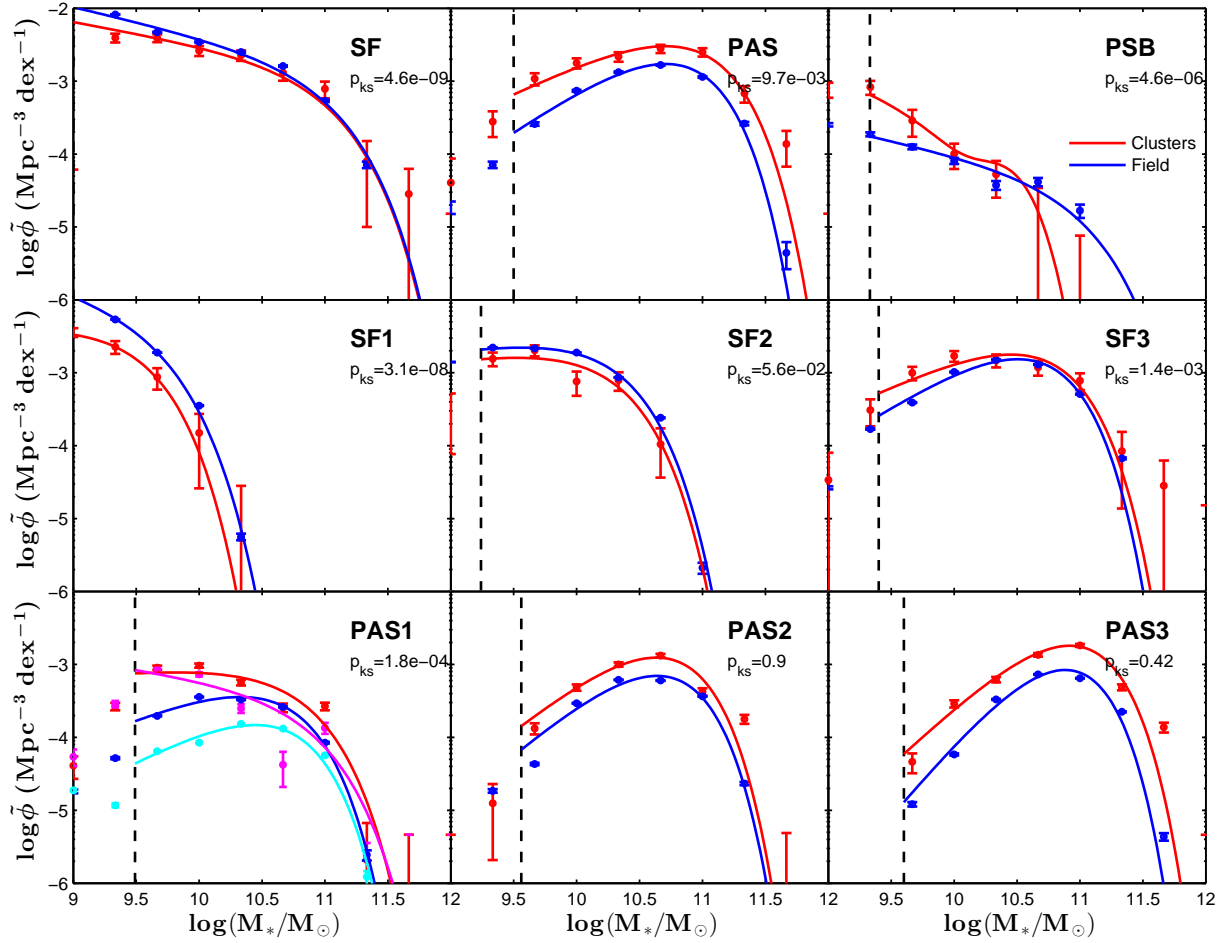


**Figure 6.** Stellar mass functions of galaxies in clusters (red) and the field (blue) at  $0.5 < z < 1.0$ . The cluster mass functions are normalised so that the total (integrated) density of galaxies matches the field. The first row corresponds to the three main galaxy populations: SF, PAS and PSB, from left to right. The second and third rows represent the mass functions of the three sub-populations of the SF and PAS categories, respectively, ordered from young to old (from left to right). In the panel corresponding to the PAS1 population, the stellar mass functions of galaxies quenched during the redshift interval  $0.5 < z < 1.0$  are represented with magenta and cyan lines for cluster and field, respectively. The vertical dashed black line indicates the 90% mass completeness limit. Additionally, each panel shows the probability that the field and cluster samples are drawn from the same underlying population, according to a KS test, as applied to the sample before statistical background subtraction.

$1.0 \times 10^{-11}$  for the low and high richness bins, respectively. Additionally, we find that the crossover point between the SF1 and PAS populations scales with richness, as expected if galaxy clusters are roughly self-similar.

PSBs are found to favour the dense cluster environment, and within 500 kpc the fraction of these galaxies is several times higher than the field. Although PSBs do not follow a clear radial trend, a KS test applied on the radial distributions reveals that formally their cluster-centric distances cannot be distinguished from those of the passive population (Table 3). There is some evidence, however, that PSBs are not as concentrated in the core region as PAS galaxies. This is broadly consistent with Muzzin et al. (2014), who found that PSBs reside in the inner volumes of clusters but avoid the very central region. We note, however, that they also showed that this trend weakens and the PSBs mimic the distribution of quiescent galaxies when line-of-sight velocity is omitted.

The radial distributions of SF1, SF2 and SF3, shown in Fig. 8, show a strong dependence of sSFR with cluster-

centric radius. The population with the highest sSFR, SF1, presents a strong radial gradient, avoiding the inner regions of clusters. SF2s exhibit a rather flat radial profile which drops in the innermost bins. Finally, SF3s are the only SF population whose fraction is higher in clusters than in the field, although the profile is flat, similar to the SF2s.

In conclusion, the radial profiles show a pattern suggesting the more passive populations (PAS, PSB and SF3) are more common in dense environments than in the field and prefer to inhabit small and intermediate cluster-centric radii. In contrast, high-sSFR galaxies avoid the central regions of clusters.

## 6 DISCUSSION

In this work we present the following observational evidence, indicating that dense environments have a substantial impact on galaxy evolution in the redshift range  $0.5 < z < 1.0$ :

- (i) There is a high abundance of low-mass passive galaxies

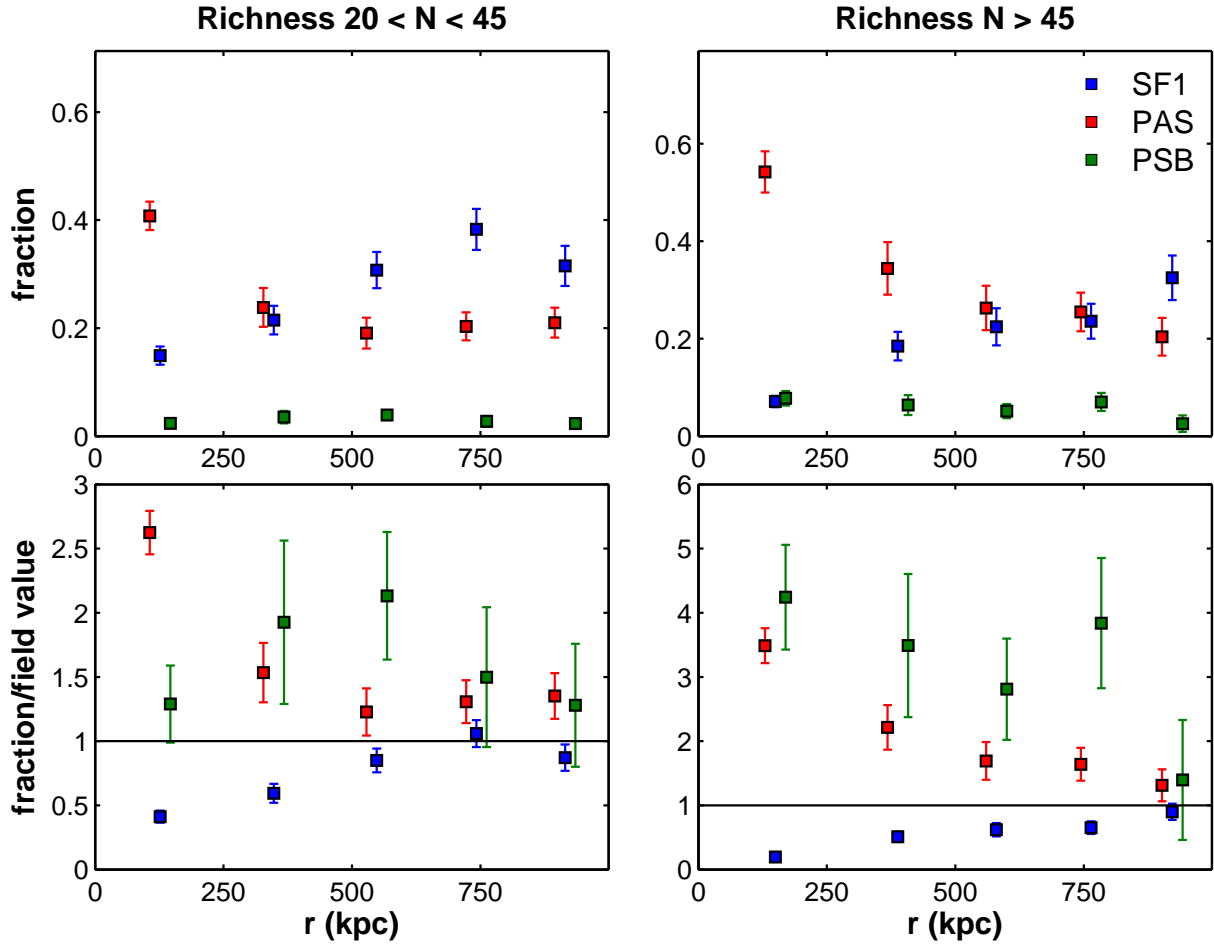


**Figure 7.** Radial plots of SF1, PAS and PSB galaxies in two cluster richness bins: clusters with between 20 and 45 FoF selected members. In the top row the fraction of each population is represented as a function of cluster-centric distance. In the bottom row the fraction is normalised by the corresponding value in the field.

and PSBs in clusters (Fig. 6), and a corresponding suppression of galaxies with high sSFR (particularly the SF1 class) compared to the field (Fig. 6 & 7). This general trend can also be seen in the distribution of galaxies in supercolour space (SC1 vs SC2; see Fig. 5), which shows that the cluster galaxy sample is skewed towards populations with lower sSFR.

(ii) There are strong radial gradients of passive and star forming fractions with cluster-centric distance. Passive galaxies dominate the central region of clusters where the galaxy density is higher, while star-forming galaxies prefer the outskirts (Fig. 7 & 8). In particular, galaxies with high sSFR (SF1) show the steepest radial gradients.

In the analysis below we use the stellar mass functions to estimate the evolutionary connection between the various galaxy populations, and in particular the contribution due to quenching in dense environments. We then identify the most likely quenching pathways, which we describe with a simple evolutionary model.

### 6.1 Contributions and timescales

In this section we estimate the contribution of each population to the descendant class due to environmental processes.

To achieve this we match the shapes of the stellar mass functions. This can be done because the SC classified galaxies correspond to 92.7% of the total sample (the rest correspond to rarer dusty, metal-poor or non-classified galaxies), so we assume that they evolve from one population to another without missing a significant fraction.

In the absence of enhanced quenching processes, we may consider a “slow fading” route, driven by the gradual decay of sSFR as galaxies build up stellar mass, which qualitatively agrees with the observed shift towards higher mass as galaxies age (see Fig. 6). In contrast, environmental processes are thought to act rapidly (Muzzin et al. 2012; Wetzel et al. 2012, 2013; Mok et al. 2013), so that galaxies do not build up a significant amount of stellar mass in the process of being quenched. In this scenario, galaxies migrate to a different population while the shape of the original mass function remains unchanged. Therefore, there are two processes that contribute to the build up of the cluster mass function according to this simple evolutionary scheme; accretion of field galaxies of the same type, and injection of galaxies from other populations due to the action of the environment. Consequently, some cluster mass functions are composites of other populations, while this is not the case in the field.

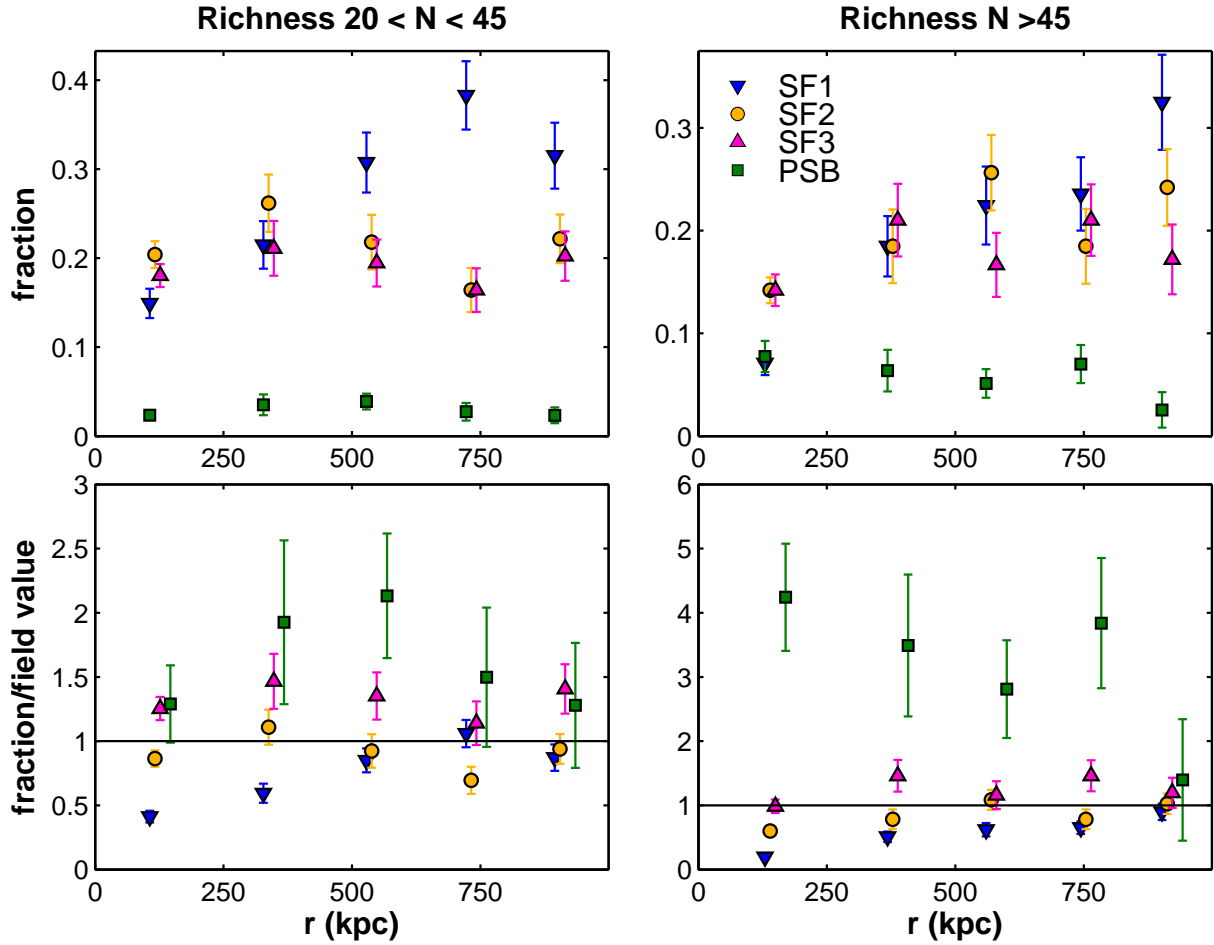


**Figure 8.** Radial plots of SF1, SF2 and SF3 galaxies in two cluster richness bins: clusters with more than 20 and fewer than 45 and clusters with more than 45 FoF selected members. In the first row the fraction of each population is represented while in the second one the fraction is normalised by the value in the field.

We estimate the composition of the cluster populations by fitting each stellar mass function with a simple model (see Equation 6), consisting of a linear combination of other populations<sup>3</sup>,

$$\tilde{\phi}_{\text{Cluster}}^i = \alpha \phi_{\text{Field}}^i + \sum_j \beta_j \phi_{\text{Field,Cluster}}^j \quad (6)$$

where  $\phi$  are the various galaxy mass functions. The subindex  $i$  corresponds to the population we are trying to model and the subindex  $j$  to all the possible contributors. The terms  $\alpha$  and  $\beta$  represent the relative contributions of the progenitor classes to the target population. The fitting is conducted using a Monte-Carlo method, minimising  $\chi^2$  while the data points are allowed to vary within errorbars.

The key assumption made when using equation 6 is that quenched galaxies do not experience rejuvenation, i.e. there is no flow of galaxies from PAS and PSB populations towards the SF class, or from PAS galaxies into PSBs. Additionally, PSBs and SF3s are the only populations that

share a boundary with the passive sequence (in the SC-diagram, see Fig. 1). Hence, in order to become passive a galaxy must evolve across this boundary. Therefore we only consider these two populations as contributors to the PAS populations. We assume the field SF mass function is the population being quenched, i.e. we assume these galaxies are quenched when they enter a cluster environment.

No assumption is made regarding the progenitors of cluster PSBs, hence all SF and field PSBs are considered potential candidates and introduced in Eq. 6. We find that the shape of the cluster PSB mass function is recovered if  $96.1 \pm 7.1\%$  of its galaxies are accreted from the SF1 class and  $3.8 \pm 0.7\%$  are accreted from the field PSB population. This is because field SF1 galaxies are the only population with a similar shape to cluster PSBs, i.e. steep at the low-mass end. The contributions from SF2s and SF3s are less than 1% (see Table 4).

We also include all the SF populations in order to reproduce the cluster SF3 mass function. We find that the excess of low-mass SF3s in clusters is reproduced by adding a contribution solely from the SF2 population, with  $12.6 \pm 3.7\%$  of cluster SF3s evolving from field SF2s, while accretion from field SF3s accounts for the remaining  $87.1 \pm 3.8\%$ . The field SF1 mass function does not provide a good fit to the cluster

<sup>3</sup> As an important caveat, we note that this model does not allow for effects of merging, which would imply evolution from one population to another with a significant change in stellar mass.

**Table 2.** Schechter parameters of all 9 galaxy population mass functions. We use single Schechter functions except for the cluster PSBs.  $M^*$  units are given in solar masses and  $\phi^*$  in  $\text{Mpc}^{-3}\text{dex}^{-1}$ . The variable  $\xi$  represents the relative change in normalisation of a cluster with respect to the field. The last two entries (\*) correspond to the mass functions of galaxies quenched at  $0.5 < z < 1.0$ , while the rest correspond to the entire sample.

		Cluster	Field
SFT	$\alpha$	$-1.310 \pm 0.010$	$-1.402 \pm 0.006$
	$\log M^*$	$10.914 \pm 0.025$	$10.930 \pm 0.010$
	$\log \phi^*$	$(-3.140 \pm 0.003)\xi$	$-3.118 \pm 0.002$
PAS	$\alpha$	$-0.170 \pm 0.022$	$0.183 \pm 0.013$
	$\log M^*$	$10.787 \pm 0.015$	$10.633 \pm 0.006$
	$\log \phi^*$	$(-2.455 \pm 0.056)\xi$	$-2.699 \pm 0.032$
PSB	$\alpha_1$	$-1.493 \pm 0.113$	$-1.378 \pm 0.027$
	$\log M^*$	$9.789 \pm 0.071$	$10.903 \pm 0.039$
	$\log \phi_1^*$	$(-3.624 \pm 0.033)\xi$	$-4.879 \pm 0.009$
	$\alpha_2$	$2.448 \pm 0.297$	
	$\log \phi_2^*$	$(-4.902 \pm 0.053)\xi$	
SF1	$\alpha$	$-0.804 \pm 0.047$	$-1.448 \pm 0.020$
	$\log M^*$	$9.334 \pm 0.020$	$9.539 \pm 0.010$
	$\log \phi^*$	$(-2.653 \pm 0.002)\xi$	$-2.444 \pm 0.006$
SF2	$\alpha$	$-0.739 \pm 0.029$	$-0.726 \pm 0.015$
	$\log M^*$	$10.108 \pm 0.022$	$10.125 \pm 0.009$
	$\log \phi^*$	$(-2.892 \pm 0.017)\xi$	$-2.745 \pm 0.009$
SF3	$\alpha$	$-0.192 \pm 0.028$	$0.103 \pm 0.016$
	$\log M^*$	$10.546 \pm 0.017$	$10.462 \pm 0.007$
	$\log \phi^*$	$(-2.688 \pm 0.063)\xi$	$-2.745 \pm 0.067$
PAS1	$\alpha$	$-0.859 \pm 0.025$	$-0.286 \pm 0.026$
	$\log M^*$	$10.659 \pm 0.024$	$10.473 \pm 0.014$
	$\log \phi^*$	$(-3.291 \pm 0.013)\xi$	$-3.394 \pm 0.039$
PAS2	$\alpha$	$0.393 \pm 0.036$	$0.488 \pm 0.025$
	$\log M^*$	$10.488 \pm 0.018$	$10.466 \pm 0.008$
	$\log \phi^*$	$(-2.864 \pm 0.040)\xi$	$-3.130 \pm 0.022$
PAS3	$\alpha$	$0.640 \pm 0.038$	$1.082 \pm 0.027$
	$\log M^*$	$10.704 \pm 0.016$	$10.564 \pm 0.007$
	$\log \phi^*$	$(-2.746 \pm 0.026)\xi$	$-3.197 \pm 0.011$
PSB*	$\alpha_1$	$-1.616 \pm 0.282$	$-2.010 \pm 0.035$
	$\log M^*$	$9.547 \pm 0.113$	$10.984 \pm 0.081$
	$\log \phi_1^*$	$(-3.544 \pm 0.076)\xi$	$-6.145 \pm 0.008$
	$\alpha_2$	$1.549 \pm 0.437$	
	$\log \phi_2^*$	$(-4.902 \pm 0.123)\xi$	
PAS1*	$\alpha$	$-1.253 \pm 0.022$	$-0.071 \pm 0.039$
	$\log M^*$	$10.792 \pm 0.027$	$10.477 \pm 0.017$
	$\log \phi^*$	$(-3.765 \pm 0.008)\xi$	$-3.760 \pm 0.239$

**Table 3.** The p-value of a KS-test when applied to radial distributions of different populations.

	$20 < N < 45$		$N > 45$	
	SF1	PSB	SF1	PSB
PAS	$4.1 \times 10^{-11}$	0.23	$8.0 \times 10^{-11}$	0.69
PSB	0.036	-	$1.9 \times 10^{-3}$	-

**Table 4.** The estimated contribution to the cluster galaxy populations (1st column) from the progenitor classes, based on fitting the galaxy mass functions (see Equation 6). Contributions are expressed as fractions of the progenitor and the target populations. Those entries marked with (f) correspond to the field, otherwise they represent cluster populations. The third column corresponds to the contribution relative to the progenitor populations, while the fourth column represents the fraction of the final population that comes from each progenitor class.

	$\Phi$	Contribution	%
PSB*	SF1(f)	$\beta = 0.11 \pm 0.01$	$96.1 \pm 7.1\%$
	SF2(f)	$\beta \sim 10^{-4}$	$< 1\%$
	SF3(f)	$\beta \sim 10^{-5}$	$< 0.1\%$
	PSB*(f)	$\alpha = 0.23 \pm 0.04$	$3.8 \pm 0.7\%$
SF3	SF1(f)	$\beta = 0.013 \pm 0.005$	$< 1\%$
	SF2(f)	$\beta = 0.12 \pm 0.04$	$12.6 \pm 3.7$
	SF3(f)	$\alpha = 1.4 \pm 0.2$	$87.1 \pm 3.8\%$
PAS1*	SF3	$\beta = 0.22 \pm 0.02$	$26.6 \pm 3.1\%$
	PSB	$\beta = 3.41 \pm 0.45$	$73.3 \pm 3.0$
	PAS1*(f)	$\alpha = 0.02 \pm 0.01$	$< 1\%$

\* Galaxies quenched at  $0.5 < z < 1.0$  selected using mean stellar age information.

SF3 mass function, implying that essentially all environmentally quenched SF1s evolve through the PSB route.

In order to estimate the visibility time of the PSB phase, we first apply the analysis to the subset of the younger PAS1 galaxies that were quenched over the redshift range  $0.5 < z < 1.0$  (magenta and cyan lines in Fig. 6). These galaxies are selected at a given redshift based on their mean stellar age, as obtained from the SC fitting procedure (see Section 2.3). As mentioned previously, we only consider cluster PSBs, cluster SF3s and field PAS1 as potential progenitors for the PAS galaxies. The similarity in shape of the cluster SF3 and field PAS1 mass functions does lead to some degeneracy affecting the contributions of these populations. This does not affect the contribution from PSBs, however. We find that  $73.3 \pm 3.0\%$  of the cluster PAS1 population that were quenched in the redshift range  $0.5 < z < 1.0$  come from cluster PSBs (with the remaining  $26.6 \pm 3.1\%$  from cluster SF3s).

We use these contributions to estimate the visibility timescale ( $\tau_{\text{vis}}$ ) for the PSB phase. The redshift range  $0.5 < z < 1.0$  corresponds to a time interval  $\Delta t = 2.7 \pm 0.3$  Gyr. The visibility timescale is calculated dividing  $\Delta t$  by the expected number of times the observed PSB population has evolved into PAS1 galaxies during this time interval (i.e.  $\beta_{\text{PSB}}$ ).

$$\tau_{\text{vis},j} = \frac{\Delta t}{\beta_j} \quad (7)$$

Expressed in terms of the parent population, the PSB contribution to PAS1s corresponds to  $3.41 \pm 0.45$  times the observed number of PSBs in clusters. This means that more than three times the current number of these galaxies must have faded into the red sequence over a time period of  $\sim 2.7$  Gyrs. Therefore, the visibility time for PSBs is  $0.8 \pm 0.1$  Gyrs.

In Section 6.3 we explore the visibility time for the PSB phase from a theoretical perspective, using stellar population

synthesis models (Wild et al. 2016). These simulations estimate visibility times between 0.4–1 Gyrs, consistent with the estimates obtained using stellar mass functions.

## 6.2 Evolutionary pathways

We now develop a simple evolutionary model to link the various populations considered in this paper.

We assume that the evolution of low-mass galaxies ( $M < 10^{10.5} M_{\odot}$ ) in the field at  $z < 1$  is mainly dominated by slow, undisturbed evolution. An isolated star-forming galaxy builds up stellar mass so that the sSFR drops and the galaxy slowly fades and moves through the star-forming classes (SF1, SF2, SF3) to eventually become passive (PAS). This slow fading is shown by the green arrows in Fig. 9. In order to produce the bulk of the PSB population additional (rapid) quenching mechanisms are needed.

We suggest that the cluster environment causes the deviations from the slow fading path. Based on the contributions calculated in Section 6.1, we conclude that this can happen in two ways. Rapid quenching affects galaxies with very high sSFR (SF1), which are quenched rapidly during infall, giving rise to PSBs. This explains the sharp up-turn of the PSB stellar mass function at the low-mass end, which matches the field SF1 mass function. Secondly, galaxies with intermediate sSFRs (SF2) may also be quenched, causing them to prematurely evolve into SF3 galaxies. These environmentally-driven paths are represented with red arrows in Fig. 9. After quenching has taken place all galaxies converge to the quiescent population, regardless of the quenching pathway they followed. First they evolve to the youngest passive population (PAS1), then progressively evolve into PAS2 and PAS3 as they age and/or dry-merge.

We now analyse the insight provided by the radial distributions, which in principle can probe the location of the environmental quenching and constrain the likely timescales. The SF1 population is found to be strongly depleted in the cluster core; a KS test confirms its distribution is inconsistent with a flat distribution ( $p_{KS} \sim 10^{-5}$ ). This implies that the timescale for this quenching process is short, and less than the typical dynamical timescale of clusters ( $< 10^9$  years), as otherwise the radial trend would dilute. In contrast, neither the SF2 or SF3 populations show strong radial trends ( $p_{KS} \sim 0.24$ ). Therefore the second evolutionary path must be a more gradual process and take longer than the dynamical timescale, i.e.  $\gtrsim 10^9$  years.

Finally, we note that PSBs show no strong radial gradients, which implies that either environmental quenching occurs everywhere within the inner Mpc of the cluster, or the visibility time of the PSB phase is comparable to the dynamical timescale,  $\sim 1$  Gyr. As noted above, however, the quenching timescale to convert SF1 galaxies into PSBs must be considerably shorter.

In summary, our results suggest more than one quenching mechanism acting in clusters, which seem to act on different timescales. One of them preferentially influences low-mass galaxies with high sSFR, while a second quenches galaxies with intermediate sSFRs.

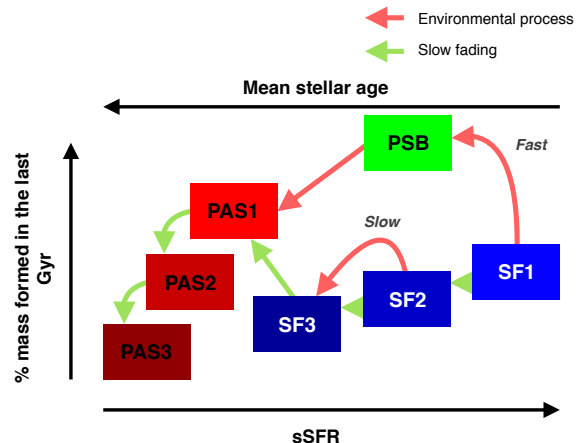


**Figure 9.** Scheme of our proposed evolutionary pathways. Green arrows illustrate the evolution of galaxies with constant SFR while the red arrows represent evolution driven by environment i.e. SFR being truncated by some environmental mechanism.

## 6.3 PSB in clusters and the field

The properties of PSB galaxies within clusters differ from PSBs in the field: their distribution in SC1–SC2 space is different as well as their mass functions. This suggests PSB galaxies may be produced through different processes depending on the environment.

To analyse the possible origins of PSB galaxies we use the stellar population synthesis models presented in Wild et al. (2016). These models consist of three different star formation histories (SFH; see Fig. 10): (1) with constant SFR, corresponds to unaltered evolution and a gradual drop in sSFR (solid line); (2) exponentially declining SFH with a decay time of 100 Myrs, representing galaxies that have undergone a strong burst of star formation that is rapidly truncated due to depletion of the gas reservoir (dotted line); and (3) exponential truncation of star formation with decay time of 400 Myrs after an extended period of continuous star formation of 1, 3 and 6 Gyrs since formation (dashed lines). In our case, this rapid truncation is assumed to be the effect of environmental quenching.

We see that the last two SFHs can lead to a PSB phase. In either case the maximum value of SC2 reached depends on the rapidity of the quenching event and the fraction of the stellar mass built up during the last Gyr. Hence PSBs formed immediately after a starburst event systematically reach higher values of SC2 than PSBs which were quenched after a more extended episode of star formation.

The distribution of PSBs in the SC diagram (Fig. 5 described in Section 5.1) suggests that PSBs are triggered by different mechanisms in different environments. In particular, those PSBs in clusters are unlikely to be produced after a significant starburst, in which the galaxy formed a considerable fraction of its stellar mass. Instead, they are more likely to have originated via rapid quenching after an extended period of star formation or after a more marginal burst of star formation. We find that PSBs in clusters are concentrated at  $SC2 < 10$  while in the field they reach much higher values ( $SC2 \sim 15$ ; see Fig. 5). In addition, this quenching must be fast ( $\tau_Q \sim 400$  Myrs, from simulations) to cause a galaxy

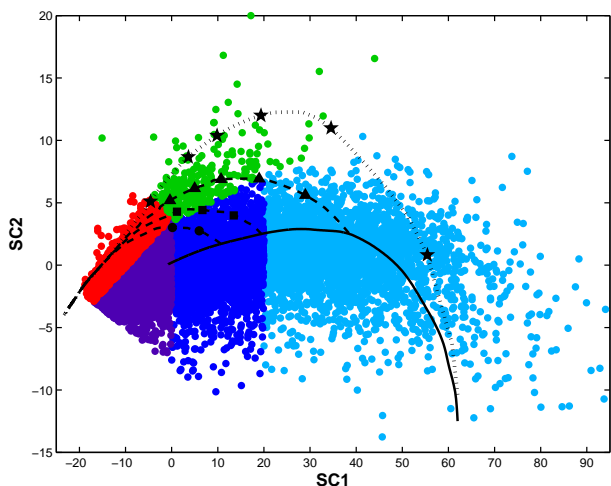


**Figure 10.** Evolutionary tracks in supercolour space, based on the Bruzual & Charlot (2003) models used in Wild et al. (2016). Filled circles represent the galaxies in our sample and their colours correspond to the population they belong to (Fig. 1). The solid line traces the evolution with constant SFR. The dotted line represents an exponentially decaying SFR with a timescale of 0.1 Gyr. Dashed lines correspond to continuous SFR and exponential truncation (with a timescale of 400 Myr) of the star formation at different times: 1, 3 and 6 Gyr after formation. Black symbols mark intervals of 0.2 Gyr starting when the SFR first drops.

to leap off the slow evolution path into the PSB regime. With much longer SFR decay times the evolution would be indistinguishable from the undisturbed case. This matches the quenching timescale  $< 1$  Gyr suggested by the radial gradient of SF1 galaxies in clusters.

Additionally, the models show that the visibility time of the PSB phase is longer if a higher value of SC2 is reached. Hence, those preceded by a starburst tend to have longer visibility times than those produced by rapid truncation after more extended star formation. Similarly, if the episode of star formation carries on for too long before being truncated, the galaxy will not reach the PSB regime at all. These two factors constrain the value of the PSB visibility timescale to the range  $0.4 < \tau_{\text{vis}} < 1$  Gyr.

In conclusion, PSBs in galaxy clusters are more likely to be produced via rapid truncation after an extended period of star formation or after a minor starburst rather than being the result of a major starburst. Simulations confirm, regardless of the underlying process, that the quenching must act quickly to produce the PSB imprint, otherwise galaxies would stay too close to the undisturbed evolutionary pathway.

#### 6.4 Mechanisms that can cause fast- and slow-quenching

Our results suggest that cluster galaxies at  $0.5 < z < 1$  quench via at least two different pathways. A single mechanism may be responsible, which affects galaxies differently depending on their properties, or several quenching mechanisms may act simultaneously to produce the different evolutionary sequences.

One pathway, which we refer to as ‘fast-quenching’, acts on short timescales, quenching galaxies faster than a cluster

dynamical time. It predominantly affects galaxies with high sSFRs and is more efficient at quenching low-mass galaxies. It becomes significant at cluster-centric radii  $R \lesssim 750$  kpc. The other pathway, which we label ‘slow-quenching’, acts on longer timescales, comparable to or greater than the cluster dynamical timescale ( $\tau_{\text{slow}} \gtrsim 1$  Gyr). Slow quenching predominantly affects galaxies which exhibit moderate sSFRs, and shows no trend with stellar mass nor cluster-centric radii.

We consider it unlikely that the enhanced quenching in clusters is produced by internal galaxies processes, such as AGN or stellar feedback. Powerful AGN feedback is generally believed to occur in massive galaxies, so it is unlikely to cause the fast-quenching described above, which is more efficient at quenching low mass galaxies. Furthermore, star-formation-driven winds are also unlikely to be the primary cause, as Fig. 10 shows no evidence for strong starbursts in cluster galaxies.

The main contenders for the mechanisms responsible for fast- and slow-quenching are interactions between the ICM and galaxies (such as ram pressure stripping and strangulation), and galaxy-galaxy interactions (such as harassment, mergers and tidal interactions).

Ram pressure stripping of the cold gas reservoir within a galaxy can quench star formation in a few hundred Myrs (Steinhauser et al. 2016). This mechanism acts preferentially in the central region of galaxy clusters or groups (Rasmussen et al. 2006; Kawata & Mulchaey 2008), where the ICM is densest and galaxies have high velocities. Furthermore, ram pressure stripping removes the cold gas reservoirs of low-mass galaxies more efficiently than high-mass galaxies as their lower gravitational potential is unable to keep the gas bound against the ram pressure. These characteristics can produce the observed properties of the fast-quenching mode described above, so ram pressure stripping is one of the contenders for causing the fast-quenching in clusters.

Galaxy mergers may also quench galaxies quickly. A merger can funnel gas into the centre of a galaxy, triggering a nuclear burst of star formation that may deplete the gas reservoir in a fraction of a Gyr. Although the merger cross section is small in the centre of clusters (Ostriker 1980; Makino & Hut 1997), these encounters frequently occur in cluster outskirts, as well as in groups. Our cluster sample is likely to have a broad range of velocity dispersions. By comparing our sample with the X-ray sample from Finoguenov et al. (2010) we estimate the majority of our structures have velocity dispersions of  $\sigma_v = 300 - 500 \text{ km s}^{-1}$ , so mergers may be frequent. However, the only type of merger able to produce the PSB stellar mass distribution is a major merger between two low-mass galaxies (i.e. two SF1s) and the resulting starburst would cause a high value of SC2, that is inconsistent with the typical values of SC2 found in cluster PSBs. Therefore, some external mechanism (e.g. gas stripping by ICM) may be required to decrease the gas fraction present in these galaxies in order to prevent a major starburst from occurring.

Galaxy encounters which cause tidal interactions, such as galaxy harassment, are much more frequent in groups and clusters than mergers, and these processes can strip gas from galaxies and reduce their SFR. Due to the high relative velocities of galaxies in clusters, these interactions are too quick and inefficient to be the direct cause of fast-quenching

evolution (Boselli & Gavazzi 2006; Byrd & Valtonen 1990), but they may be responsible for slow-mode quenching.

At this point we are unable to pinpoint the mechanism that produces the fast-quenching within  $0.5 < z < 1$  clusters. However, future studies of the morphology of cluster PSBs may shed some light on which mechanism is responsible. Mergers would produce PSBs with disturbed/spheroidal morphologies, as the interaction disrupts the structures of the galaxies, whilst ram pressure stripping/strangulation would result in PSBs with more disc-like morphologies, as the galaxy would quench before the disc fades.

Many of the features exhibited by the slow-quenching mechanism can be explained by galaxy strangulation, where the hot gas envelope of the galaxy is removed by the ICM. For example, strangulation halts star formation gradually over  $\sim 4$  Gyrs (Bekki et al. 2002). The hot gas reservoir of a galaxy is easily removed through interactions with the ICM, therefore strangulation affects both high and low-mass galaxies equally.

However, there are other potential processes responsible for slow-quenching. Galaxy harassment, as mentioned before, could significantly affect the star formation of a galaxy after a number of encounters, which requires a few Gyrs. Similarly, mergers involving galaxies with low gas content and intermediate sSFRs (SF2) may quench galaxies without following the PSB route.

## 7 CONCLUSIONS

We have optimised a Friends-of-Friends algorithm to find galaxy overdensities in the UKIDSS UDS field, allowing us to analyse the relationship between environment and galaxy quenching. In the redshift range  $0.5 < z < 1.0$  we identify 37 candidate galaxy clusters containing at least 20 galaxies. To analyse the field and cluster galaxy populations, we use the PCA galaxy classification scheme of Wild et al. (2016), which allows us to separate star-forming, passive, and recently-quenched “post-starburst” (PSB) galaxies using photometric data. Comparing the resulting stellar mass functions, and the radial distributions for cluster populations, our key findings can be summarised as follows:

(i) We find evidence for an overabundance of low-mass passive galaxies and PSBs in galaxy clusters compared to less dense environments. The PSB population show a very steep stellar mass function in clusters, dominated by galaxies at low mass ( $M < 10^{10} M_{\odot}$ ).

(ii) Galaxy clusters show a relative underabundance of galaxies with high specific star-formation rates (SF1 galaxies). The SF1 mass function is steep, suggesting that rapid quenching of this population in dense environments provides a natural explanation for the corresponding excess of PSBs.

(iii) The radial distribution of galaxy types reveals a decline in the fraction of star-forming galaxies towards cluster cores, with a corresponding steep rise in the passive galaxy population. The SF1 population show a very steep decline towards cluster cores, suggesting very rapid quenching of these galaxies on entering dense environments, on a timescale less than the cluster dynamical timescale ( $< 1$  Gyr).

(iv) We measure a typical visibility time for the PSB

phase of galaxies within clusters of  $800 \pm 100$  Myrs, based on a comparison of stellar mass functions.

(v) We find that PSBs in galaxy clusters are most likely to be produced by a rapid truncation following an extended period of star formation or after a minor starburst, rather than gas depletion after a major starburst. This may imply that environmental mechanisms typically quench galaxies without triggering any significant burst of star formation.

To explain the relative abundances and radial distributions, we suggest there are two main quenching pathways occurring in clusters: rapid quenching and slow quenching. The first path affects galaxies with high sSFR (SF1), predominantly at low mass, which quench rapidly to become PSBs and thereafter build up the low-mass end of the passive red sequence. The second pathway affects star-forming galaxies with moderate sSFR (SF2), accelerating their decay in sSFR over an extended period of time, comparable to the dynamical timescale of a galaxy cluster.

The processes behind fast environmental quenching need to act on timescales shorter than 1 Gyr, quench preferentially high sSFR/low-mass galaxies, and produce a strong radial dependence without inducing a strong starburst. Ram-pressure stripping provides a likely explanation, although we cannot rule out a contribution from other processes (such as merging). Similarly, the processes behind slow quenching act on timescales comparable to the cluster dynamical time or longer, affecting galaxies with intermediate sSFR regardless of their stellar mass. Such trends can be explained through strangulation, gradual galaxy harassment, or gas-poor mergers.

In summary, we conclude that environmental processes appear to have a significant impact on the properties of low-mass galaxies in the redshift range  $0.5 < z < 1.0$ .

## 8 ACKNOWLEDGEMENTS

This work uses data from ESO telescopes at the Paranal Observatory (programmes 094.A-0410 and 180.A-0776; PI: Almaini). We are grateful to the staff at UKIRT for their tireless efforts in ensuring the success of the UDS project. We also wish to recognize and acknowledge the very significant cultural role and reverence that the summit of Mauna Kea has within the indigenous Hawaiian community. We were most fortunate to have the opportunity to conduct observations from this mountain. MS acknowledges support from IAC and STFC. VW acknowledges support from the European Research Council Starting grant (SEDmorph, P.I. V. Wild). We also use data from the VIMOS Public Extragalactic Redshift Survey (VIPERS). VIPERS has been performed using the ESO Very Large Telescope, under the “Large Programme” 182.A-0886. The participating institutions and funding agencies are listed at <http://vipers.inaf.it>.

## REFERENCES

- Akiyama M., et al., 2015, *PASJ*, 67, 82
- Balogh M., et al., 2004, *MNRAS*, 348, 1355
- Bamford S. P., et al., 2009, *MNRAS*, 393, 1324
- Bekki K., Couch W. J., Shioya Y., 2002, *ApJ*, 577, 651

- Best P. N., Kauffmann G., Heckman T. M., Brinchmann J., Charlot S., Ivezić Ž., White S. D. M., 2005, *MNRAS*, 362, 25
- Blake C., et al., 2004, *MNRAS*, 355, 713
- Boselli A., Gavazzi G., 2006, *PASP*, 118, 517
- Brammer G. B., van Dokkum P. G., Coppi P., 2008, *ApJ*, 686, 1503
- Bruzual G., Charlot S., 2003, *MNRAS*, 344, 1000
- Byrd G., Valtonen M., 1990, *ApJ*, 350, 89
- Chabrier G., 2003, *PASP*, 115, 763
- Chuter R. W., et al., 2011, *MNRAS*, 413, 1678
- Cooper M. C., et al., 2007, *MNRAS*, 376, 1445
- Cooper M. C., et al., 2008, *MNRAS*, 383, 1058
- De Lucia G., Weinmann S., Poggianti B. M., Aragón-Salamanca A., Zaritsky D., 2012, *MNRAS*, 423, 1277
- Dekel A., Birnboim Y., 2006, *MNRAS*, 368, 2
- Diamond-Stanic A. M., Moustakas J., Tremonti C. A., Coil A. L., Hickox R. C., Robaina A. R., Rudnick G. H., Sell P. H., 2012, *ApJ*, 755, L26
- Dressler A., 1980, *ApJ*, 236, 351
- Dressler A., Gunn J. E., 1983, *ApJ*, 270, 7
- Eisenhardt P. R. M., et al., 2008, *ApJ*, 684, 905
- Elbaz D., et al., 2007, *A&A*, 468, 33
- Finoguenov A., et al., 2010, *MNRAS*, 403, 2063
- Font A. S., et al., 2008, *MNRAS*, 389, 1619
- Furusawa H., et al., 2008, *ApJS*, 176, 1
- Geach J. E., Simpson C., Rawlings S., Read A. M., Watson M., 2007, *MNRAS*, 381, 1369
- Geller M. J., Huchra J. P., 1983, *ApJS*, 52, 61
- Goto T., et al., 2003, *PASJ*, 55, 771
- Gunn J. E., Gott III J. R., 1972, *ApJ*, 176, 1
- Haines C. P., et al., 2015, *ApJ*, 806, 101
- Hartley W. G., et al., 2013, *MNRAS*, 431, 3045
- Hopkins P. F., Hernquist L., Cox T. J., Di Matteo T., Martini P., Robertson B., Springel V., 2005, *ApJ*, 630, 705
- Huchra J. P., Geller M. J., 1982, *ApJ*, 257, 423
- Kang X., van den Bosch F. C., 2008, *ApJ*, 676, L101
- Kauffmann G., White S. D. M., Heckman T. M., Ménard B., Brinchmann J., Charlot S., Tremonti C., Brinkmann J., 2004, *MNRAS*, 353, 713
- Kawata D., Mulchaey J. S., 2008, *ApJ*, 672, L103
- Larson R. B., Tinsley B. M., Caldwell C. N., 1980, *ApJ*, 237, 692
- Lee S.-K., Im M., Kim J.-W., Lotz J., McPartland C., Peth M., Koekemoer A., 2015, *ApJ*, 810, 90
- Makino J., Hut P., 1997, *ApJ*, 481, 83
- Maltby D. T., et al., 2016, *MNRAS*, 459, L114
- Marshall H. L., Tananbaum H., Avni Y., Zamorani G., 1983, *ApJ*, 269, 35
- Martig M., Bournaud F., Teyssier R., Dekel A., 2009, *ApJ*, 707, 250
- McGee S. L., Balogh M. L., Wilman D. J., Bower R. G., Mulchaey J. S., Parker L. C., Oemler A., 2011, *MNRAS*, 413, 996
- Merchán M. E., Zandivarez A., 2005, *ApJ*, 630, 759
- Mok A., et al., 2013, *MNRAS*, 431, 1090
- Muzzin A., et al., 2012, *ApJ*, 746, 188
- Muzzin A., et al., 2014, *ApJ*, 796, 65
- Oemler Jr. A., 1974, PhD thesis, [doi:10.1086/153216](https://doi.org/10.1086/153216)
- Ostriker J. P., 1980, *Comments on Astrophysics*, 8, 177
- Peng Y.-j., et al., 2010, *ApJ*, 721, 193
- Pozzetti L., et al., 2010, *A&A*, 523, A13
- Rasmussen J., Ponman T. J., Mulchaey J. S., 2006, *MNRAS*, 370, 453
- Scodeggio M., et al., 2016, preprint ([arXiv:1611.07048](https://arxiv.org/abs/1611.07048))
- Simpson C., et al., 2012, *MNRAS*, 421, 3060
- Simpson C., Westoby P., Arumugam V., Ivison R., Hartley W., Almaini O., 2013, *MNRAS*, 433, 2647
- Smail I., Sharp R., Swinbank A. M., Akiyama M., Ueda Y., Foucaud S., Almaini O., Croom S., 2008, *MNRAS*, 389, 407
- Steinhauser D., Schindler S., Springel V., 2016, *A&A*, 591, A51
- Tran K.-V. H., Franx M., Illingworth G., Kelson D. D., van Dokkum P., 2003, *ApJ*, 599, 865
- Ueda Y., et al., 2008, *ApJS*, 179, 124
- Vergani D., et al., 2010, *A&A*, 509, A42
- Weinmann S. M., Kauffmann G., von der Linden A., De Lucia G., 2010, *MNRAS*, 406, 2249
- Wetzel A. R., Tinker J. L., Conroy C., 2012, *MNRAS*, 424, 232
- Wetzel A. R., Tinker J. L., Conroy C., van den Bosch F. C., 2013, *MNRAS*, 432, 336
- Wheeler C., Phillips J. I., Cooper M. C., Boylan-Kolchin M., Bullock J. S., 2014, *MNRAS*, 442, 1396
- Wild V., Walcher C. J., Johansson P. H., Tresse L., Charlot S., Pollo A., Le Fèvre O., de Ravel L., 2009, *MNRAS*, 395, 144
- Wild V., et al., 2014, *MNRAS*, 440, 1880
- Wild V., Almaini O., Dunlop J., Simpson C., Rowlands K., Bowler R., Maltby D., McLure R., 2016, *MNRAS*, 463, 832
- Williams R. J., Quadri R. F., Franx M., van Dokkum P., Labbé I., 2009, *ApJ*, 691, 1879
- Yan R., Newman J. A., Faber S. M., Konidaris N., Koo D., Davis M., 2006, *ApJ*, 648, 281
- Yan R., et al., 2009, *MNRAS*, 398, 735
- van Breukelen C., et al., 2006, *MNRAS*, 373, L26
- van der Wel A., 2008, *ApJ*, 675, L13
- von der Linden A., Wild V., Kauffmann G., White S. D. M., Weinmann S., 2010, *MNRAS*, 404, 1231

This paper has been typeset from a  $\text{\TeX}/\text{\LaTeX}$  file prepared by the author.